INSTITUT DE FRANCE
Académie des sciences

Comptes Rendus
Mécanique

Chady Ghnatios, Ilige Hage and Najib Metni

Knee joint injury risk assessment by means of experimental measurements and proper generalized decomposition

Volume 349, issue 2 (2021), p. 345-369

Published online: 7 June 2021

https://doi.org/10.5802/crmeca.89

Les Comptes Rendus. Mécanique *sont membres du Centre Mersenne pour l'édition scientifique ouverte*
www.centre-mersenne.org
e-ISSN : 1873-7234

Comptes Rendus
Mécanique
2021, 349, nº 2, p. 345-369
https://doi.org/10.5802/crmeca.89

Synthese / *Synthèse*

Knee joint injury risk assessment by means of experimental measurements and proper generalized decomposition

Chady Ghnatios[*, a], **Ilige Hage**[a] **and Najib Metni**[a]

[a] Notre Dame University-Louaizé, Department of Mechanical Engineering, P.O. Box 72, Zouk Mikhael, Zouk Mosbeh, Lebanon

E-mails: cghnatios@ndu.edu.lb (C. Ghnatios), ilige.hage@ndu.edu.lb (I. Hage), nmetni@ndu.edu.lb (N. Metni)

Abstract. Human joints in general and the human knees particularly are subjected to impacts and wear on a daily basis, specifically during jumping. Considering their inefficient healing and the lack of effective replacements, knee joints became a hot topic for biomechanics research. Multiple works aim to model the knee joint behavior in the literature either experimentally or through finite elements simulations. In this work, we study the effects of the Lebanese folkloric dance Dabke jumping and compare it to vertical jumping. Moreover, we tackle the modeling and simulation of a tibiofemoral knee joint under impact using optimized inverse dynamics and the Brinkman model in the biphasic synovial joint domain. This joint model is mainly made of cartilage, a meniscus (both biphasic low permeability materials), and viscous synovial fluid. Because of the degenerated shape in the thickness direction, classical methods require a large number of degrees of freedom to correctly reproduce the knee behavior. To circumvent this problem, proper generalized decomposition (PGD) model reduction techniques are used to simulate the knee synovial joint. A smart, physically based morphing of space is used to accelerate the simulation process using model reduction techniques. The result of the work is a three-dimensional simulation of the velocity and pressure fields inside the synovial domain, as well as the loads and risks in every muscle and ligament. The experimental results are coupled to the simulations one to derive the main risks involved in both vertical jumping and Dabke jumping.

Keywords. Knee simulation, Impact, Proper generalized decomposition, Biphasic materials, Jumping risk, Shoe effect.

Manuscript received 21st April 2021, revised and accepted 21st May 2021.

1. Introduction

Human movement is the result of the combined contribution of the musculoskeletal system controlled by neural connections. A perfect balance during any activity requires a good distribution of forces among the joints, tendons, muscles, and ligaments. Therefore, the human joint reaction

* Corresponding author.

forces, result of the work of the musculoskeletal system, has been extensively studied and investigated to properly model human motion and predict injury risks. Joint reaction forces estimation literature survey dates back to the 1960's, where the forces that might be causing fractures to the proximal end of the femur were analyzed by Hirsch *et al.* [1].

Nowadays, with the newly developed musculoskeletal models using finite element or based on inverse dynamics coupled to the newly developed optimization techniques, one can estimate accurately joint reaction forces at any body part and under any activity. This was accomplished and validated through sophisticated motion capture systems equipped with force plates (e.g., Mezghani *et al.* [2]) and electromyography (EMG) system, an electrodiagnostic medicine technique (e.g., Lloyd and Besier [3]).

Several analytical methods were also developed in order to simulate joint reaction forces and pressure fields. These models helped in predicting joints contact stresses and provide an improved understanding of the load distribution in any joint either in its normal or defective state. Examples of these methods include biomechanical modeling [4], three-dimensional (3D) mathematical modeling [5], optimization techniques with different cost functions [6, 7], inverse dynamics coupled with optimization [8–10], and finite element simulation (FEM) [11, 12].

In this work, we focus mainly on the knee joint which is made of the articular cartilage, the meniscus (both biphasic materials but generally considered to be elastic in the published human knee models), and the synovial fluid. In [13], the authors modeled the tibiofemoral knee joint to be comprised of cartilage as an elastic material, ligaments as nonlinear elastic springs, and menisci as equivalent-resistance springs in 3D FEM in order to study its response to axial tibial moments of up to 10 N·m. The knee joint model in FEM in [14], included both the cortical and trabecular bone of the femur and tibia, the articular cartilage of the femoral condyles and tibial plateau, the medial and lateral menisci, the transverse ligament, the anterior cruciate ligament, and the medial collateral ligament, where solid models for the menisci and articular cartilage was adopted. The authors in [15] described the soft tissues on the knee (cartilage and meniscus) to have a complex structure as inhomogeneous and biphasic structure, exhibiting a nonlinear, time-dependent behavior. In [16], a FEM model of the knee included the fluid pressure and site-specific collagen fiber orientation in the cartilages and menisci using fibril-reinforced modeling. The authors in [17] presented a novel model of the knee joint that incorporates the nonhomogeneous cartilage and meniscus as fibrils networks in FEM.

A proper modeling of the knee joint helps in the innovation of joint replacement as was performed by the authors in [18], where a viscoelastic fluid has been considered to represent the synovial fluid and purely viscous Newtonian fluid in the porous layer are used to study the lubrication mechanism occurring in knee joint using analytical solutions in order to enhance knee joint implants. Therefore, the goal line in this research is to develop a new model of the knee joint to predict the joint reaction forces, pressure fields, as well as the forces involved in all of the joint's active muscle and ligaments, an actively investigated topic nowadays.

In this research, the focus is on the knee human joint reaction forces modeling while performing vertical jumping and the Lebanese folkloric dance Dabke. Experimental measurements are performed to compare the results of professional healthy dancers in vertical jump and Dabke jump while using a force plate to recuperate the ground reaction forces along with high-speed cameras to evaluate the position, velocity, and accelerations of different body components relevant to the study. Once the experimental results are collected, the muscles, ligaments, and joints reactions are studied using inverse analysis and optimization. As can be inferred several analytical models were developed and used to estimate muscle, ligaments and joint reaction forces for any joint in any activity with the most widely used are finite element, inverse dynamics coupled with several optimization methods. Recent works involved the use of finite elements simulation for coupled fluid–solid simulation in the knee joint [19, 20] to study the creep behavior of the

joint, using nonlinear reinforced fibers for the cartilage and meniscus. Other works show experimental tests highlight the importance of the presence of the meniscus in the knee [21]. One of the best known models to replicate the behavior of biphasic porous materials (like the meniscus) when interacting with a nonporous fluid domain is the Brinkman model [22]. In fact, Brinkman combines Darcy model for porous media and Stokes model for viscous fluids. However, the use of lubrication assumptions appeared recently as an irrational simplification in stratified domains subjected to the squeeze flow [22]. To the authors best knowledge, Brinkman's solution has never been used to model knee joint (its synovial fluid). In fact, the complexity of the model (when excluding the lubrication assumptions) and the need to use an extremely refined mesh hinders the use of such a model in classical simulations. Thus, the proper generalized decomposition (PGD) model reduction technique appears to be an appealing approach. In addition, the simulation of the knee joint has never been addressed using PGD. This research contribution covers a novel methodology to model knee human joint using the combination of inverse dynamics and numerical optimization to obtain the joint reaction forces; Brinkman equations to model the knee behavior and proper generalized decomposition model reduction technique (PGD) to solve the governing equations. The rationale behind proposing a model using Brinkman equations comes from the fact that the synovial joint is a soft biphasic material. In fact, the knee joint is made of the upper articular cartilage, lower cartilage (the meniscus), and the synovial fluid filling the cavity. Cartilage (and the meniscus) are biphasic materials made of fibrous brush impregnated with fluid [23]. It is currently believed that cartilage fluid pressurization is the main driving phenomenon of the joint reaction force during the early stage of the impact [23–25]. However, biphasic materials are challenging to model, with their effective modeling not mastered yet [26–28].

This work starts by detailing the experimental procedure used to obtain the ground reaction forces and the joints' accelerations. Using inverse dynamics coupled to a genetic optimization procedure, we obtain joint reaction forces. Later, the obtained values are leveraged to simulate the risk in a group of professional and healthy dancers comparing males and females samples. The pressure field inside the synovial joint in each individual is also obtained using the Brinkman model and PGD to alleviate the dimensionality of the problem [29, 30]. In fact, PGD alleviates the curse of dimensionality by separating the problem solution into lower dimensionality solutions [31].

2. Experimental methods and procedure

For most athletes and dancers, injuries occur at knee level since knee motion involves a series of three rotations (flexion/extension, abduction/adduction, and internal/external rotations) and three translations (anterior/posterior, superior/inferior, and medial/lateral translations). The aim of this experiment is to identify the joint's displacement, velocity, and acceleration, as well as the ground reaction force. In this experiment, a set of markers using OptiTrack Motion Capture System® (and Motive software) were placed in order to obtain the position parameters of the hip, knee, and ankle joints of the right leg so that the right knee internal joint reaction force would be calculated when the individuals are dancing the Lebanese folkloric dance Dabke specifically while having a vertical jump during the dance.

2.1. *Participants*

The experiments were conducted on six subjects (professional Dabke dancers), 3 male and 3 female with different heights, weights, and ages. All individuals were healthy professional dancers; Table 1 shows the subjects specific details and measured (both manually and through Optitrack)

Table 1. Tests and subjects specific anthropometric data

Subject number	Sex	Age	Height (cm)	Weight (kg)	Knee circumference (cm)	Shoe
1	*M*	30	172	63	34.5	No
2	*M*	44	170.5	63.1	35.5	No
3	*M*	29	180	73.84	36.5	No
4	*F*	27	160	50.4	32	No
5	*F*	21	162	47.33	33	No
6	*F*	29	161	55.8	37	No
4	*F*	27	160	50.4	32	Yes
5	*F*	21	162	47.33	33	Yes
6	*F*	29	161	55.8	37	Yes

Tests are repeated twice for vertical jumps and Dabke jump.

anthropometric data of height, weight, and knee circumference needed for the kinematics calculations. For all tests were conducted barefoot; for the girls' additional tests were conducted with an 8.5 cm heel height shoe (classically used in professional Dabke) in order to test the shoe heel height effect on the knee reaction force.

2.2. *Experimental setup*

In this study a commercial motion capture software Optitrack® was used. This system consists of eight infrared cameras (on all corners) and seven retroreflective markers. The markers are 1.5 cm in diameter and are attached to the precise anatomical locations of the participant's leg. The locations where the markers were positioned on the dancer's leg are at the hip, knee, and ankle, as shown in Figures 1(a) and (b), following the Oxford foot model used by the Optitrack tracking system, which is a default model integrated in the tracking systems:

- RFWT1: placed on the hip femur bone (greater trochanter);
- RFWT2: placed under the hip femur bone (greater trochanter);
- RTHI: placed on the outside of the thigh below hand swing;
- RKNE: placed on the outside of the knee joint;
- RSHN: placed on the outside of the lower leg;
- RANK: placed on the bony prominence on the outside of the ankle;
- RTOE: placed on the tip of the big toe.

The computerized camera system with accompanying software captures the exact motion of the retroreflective markers and thus records their trajectory while the volunteer performs the jumping over the AMTI force plate (BP400600-OP-2K-STT) 40 by 60 cm, as shown in Figure 2. The cameras were connected to a computer that acquires kinematic data.

The subjects were instructed to jump first in a vertical manner while standing on a force plate, which measures the reaction force, then to jump from the ground on the force plate in the same way they jump while dancing the Dabke. For the vertical jump, the steps are as follows:

(1) subject stands straight in front of the force plate at the marked position;
(2) initialize both the force plate and Optitrack systems;
(3) wait 5 s;
(4) subject stands on force plate;
(5) wait 2 s;
(6) subject jumps vertically and lands in a straight way on both foots;
(7) wait 2 s;

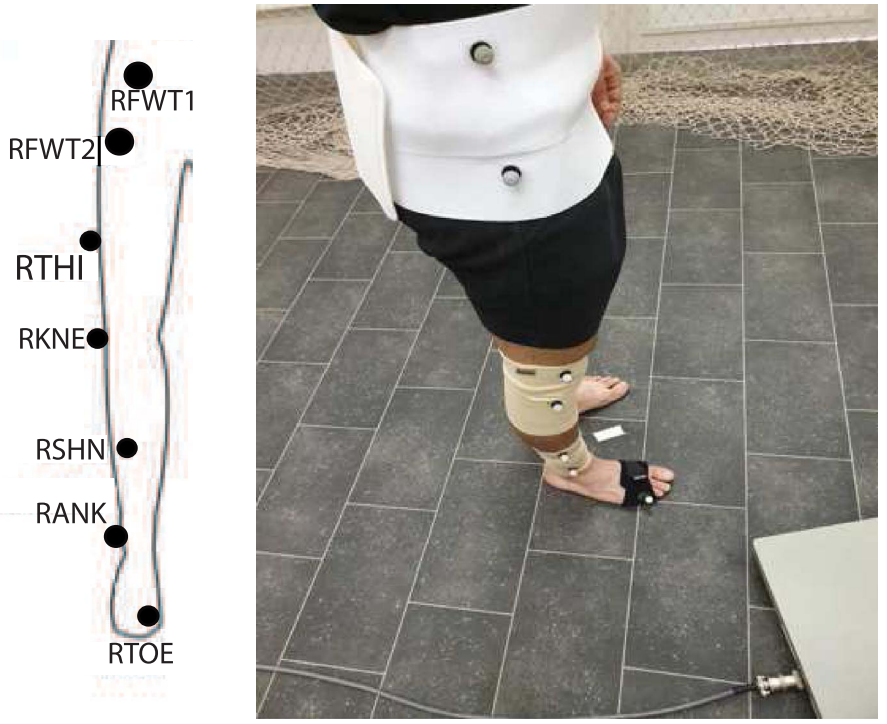

Figure 1. Position of different markers.

Figure 2. Force plate AMTI BP400600-OP-2K-STT.

(8) subjects gets off the force plate;
(9) stop recording on the PC;
(10) save PC data with correct label.

While performing Dabke, the steps are as follows:

(1) subject stands straight on the side of the force plate at the marked position;
(2) initialize both the force plate and Optitrack systems;
(3) wait 5 s;
(4) subject starts the first 2 moves of the Dabke discussed while still being on the floor;
(5) the subject does the Dabke jump landing on the force plate with the right leg;

Figure 3. Markers height from the ground of subject 1 while performing a vertical jump.

(6) the subject must not let the other leg touch the force plate;
(7) the subject gets off the force plate right after the jump;
(8) stop recording on the PC;
(9) save PC data with correct label.

The aforementioned; vertical jump and Dabke steps were repeated for each subject on barefoot or heel height as required.

2.3. *Data acquisition*

For each individual jump, the following variables were measured: frame rate, total time of experiment, 3D coordinated of the hip, knee, and ankle for every frame and the corresponding forces measured on the force plate for each contact. The Vicon system provides the x, y, and z coordinates instantaneously for each marker (which will be used to calculate the velocity, acceleration, angle, angular acceleration, and angular velocity at the knee joint). According to [32,33] measured values for marker position are influenced by noise due to the wobbling of the participant's skin. The value of this uncertainty is in range ± 2 mm. In addition, the instantaneous ground reaction force was sampled from the multiaxis AMTI force plate at the rate of 100 Hz. Before the experiment, calibration was conducted to work out the space coordinate system for the camera system field of view. The calibration was performed fully in accordance with the proposed manufacturers procedures.

2.4. *Data postprocessing*

The collected experimental results are to be used to derive the muscles, ligaments, and joint forces in the knee, as well as the attributed risk factors. Therefore, the inverse dynamics and optimization is mandatory to identify different reaction forces on different body components.

To avoid numerical artifacts, the kinematic data was first fitted over the time domain using moving least squares (MLS) [34, 35], with a fitting window dynamically refined using the actual computed gradient at the end of the previous MLS window. The displacement results of all markers for subject number 1 of Table 1 performing a vertical jump are shown in Figure 3, while his Dabke jump results are shown in Figure 4.

The fitted results are used to compute the velocity and acceleration as a function of the time using Euler's centered differences. Figures 5 and 6 show the accelerations corresponding to

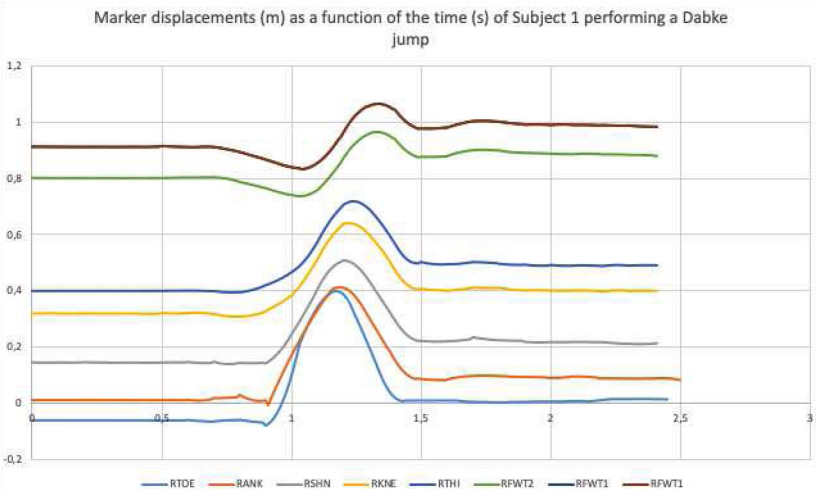

Figure 4. Markers height from the ground of subject 1 while performing a Dabke jump.

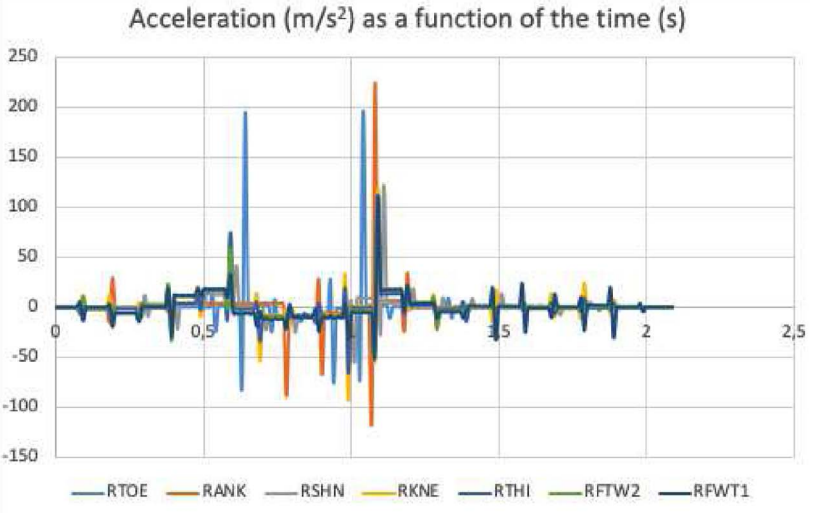

Figure 5. Vertical accelerations of the markers of Subject 1 while performing a vertical jump.

Figures 3 and 4. The acceleration figures are characterized by two high peaks, eventually related to the beginning of the motion and the impact with the force plate at the end of the motion. Later on, these results are used in the inverse dynamics and optimization to derive the muscles, ligaments, and joint forces in the knee, as well as the attributed risk factors.

3. Inverse dynamics, optimization, and risk assessment

In the inverse analysis study, we use the dynamics relations in the foot and then the leg to transmit the measured ground reaction forces to the knee joint. The anthropometric data considered are taken from [10, 36]. The inverse dynamics matrix equation is written as

$$\mathbf{M}\cdot\ddot{\mathbf{q}}+\mathbf{A}\cdot\mathbf{f}+\mathbf{B}\cdot\mathbf{g}=0, \tag{1}$$

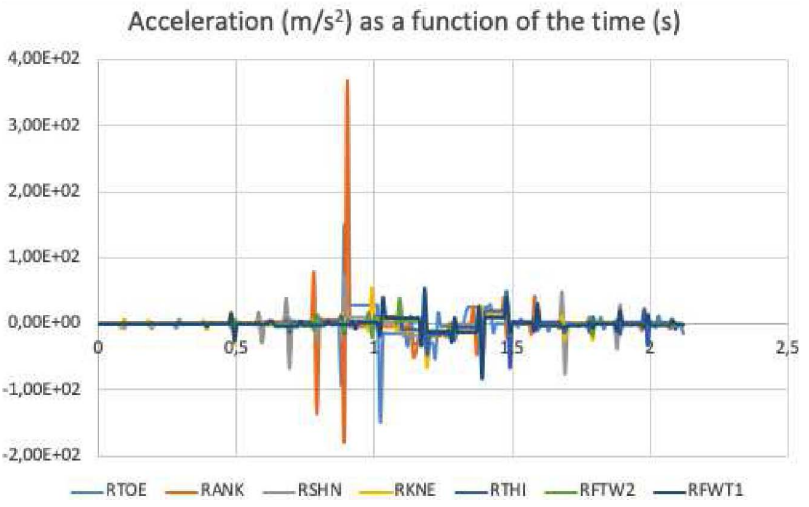

Figure 6. Vertical accelerations of the markers of Subject 1 while performing a Dabke jump.

where $\mathbf{M}$ is the mass matrix of the selected body component (leg or foot), $\ddot{\mathbf{q}}$ is the acceleration vector, $\mathbf{f}$ is the vector of unknown joint reactions, while $\mathbf{g}$ is the vector of known external forces (ground reaction forces when considering the foot, and the identified ankle forces when considering the knee). $\mathbf{A}$ and $\mathbf{B}$ are the matrices defining the moments of the reaction forces.

To find the muscles and ligaments forces, we use an optimization procedure, minimizing the risk of failure of each component [37, 38]. The allowable properties were found using the anthropometric data from the literature [39,40]. The moment arms are defined in our work using the "through points" method to find the exact orientation of the forces and the moments [39]. The considered minimization problem is written by

$$\mathbf{X} = \arg\min_{\mathbf{X}\in\mathbb{R}} \left\{ \sum_{i=1}^{i=N_1} \frac{\|\sigma_i\|^{n_1}}{\|\sigma_i^{\text{ult}}\|^{n_1}} + \sum_{i=1}^{i=N_2} \frac{\|\sigma_i\|^{n_2}}{\|\sigma_i^{\text{ult}}\|^{n_2}} + c\|\mathcal{F}_1\|^{n_3} + c\|\mathcal{F}_2\|^{n_3} \right\} \tag{2}$$

with $\mathcal{F}_1$ and $\mathcal{F}_2$ being the components of the synovial joints reaction forces on the ankle and the knee joint, respectively. The effect of the force $\mathcal{F}_2$ on the synovial joint will be studied in Section 4. The chosen fractions $\|\sigma_i\|^{n_j}/\|\sigma_i^{\text{ult}}\|^{n_j}$ consists of the inverse of the factor of safety against rupture of the corresponding muscle or ligament n_j. The cost function depicted in (2) minimizes, therefore, the computed risk and maximizing the factor of safety, for each muscle $N_1 = 22$ and ligament $N_2 = 11$ in the lower body part, under the knee. c is an optimization constant set less than 1; n_1, n_2, and n_3 are exponents defining the used norms of the risk values. The ratio of the computed stresses divided by the ultimate stresses of each muscle of ligaments are the risk of failure of each component. The ultimate stresses σ_i^{ult} are taken from the literature data [37,38]. The minimization problem is also subject to the two constraints as follows:

- Sum of the moments in the ligaments and muscles should satisfy the reaction moment on the knee and ankle as obtained from (1).
- The sum of the forces in the ligaments, muscles, and joints should satisfy the reaction forces obtained in the inverse dynamics from (1).

A genetic algorithm is used to solve the optimization problem. A matlab® graphical interface is created to ease the user inputs. The optimization algorithm converges within few minutes on a portable PC, with a cost function reduced to less than $\epsilon = 10^{-3}$.

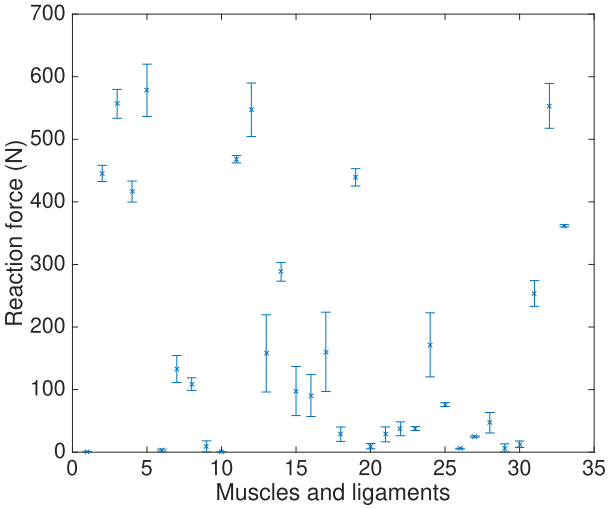

Figure 7. Average and standard deviations of muscles reactions in male subjects performing a vertical jump with a locked knee.

3.1. *Optimization results*

In this section, we consider only the instant showing the highest impact force on the force plate to illustrate the most critical load on the knee joint components. Figure 7 illustrates the average and standard deviation of the experimental results of the reactions in the muscles and ligaments for males subjects performing a vertical jump on the force plate. The ligaments and forces are referred by 1 to 33 with the corresponding names illustrated in Table A.1 in Appendix A.

We illustrate the results in term of risk factors r_i defined by the actual body component exhibited maximum stress over the ultimate stress of that body component

$$r_i = \frac{\sigma_i^{\max}}{\sigma_i^{\text{ult}}}. \tag{3}$$

Figures 8(a) and (b) illustrates the risk factors on the ligaments and muscles for the males subjects using the average values between the considered experiments, at the moment exhibiting the maximum ground reaction force.

Figures 9(a) and (b) illustrates the risk factors on the ligaments and muscles for the females subjects using the average values between the considered experiments, at the moment exhibiting the maximum ground reaction force. From Figures 8 and 9, we can conclude that vertical jump with locked knee is more critical, with higher injury risk than the Dabke dance jump, for both males and females. However, the highest risk factors in vertical jumps for males appear on the Flexor digitorum longus (component 24) and the semimembranosus muscles (component 11) in both vertical jump and Dabke, while for females, the highest risk appears on the Flexor digitorum longus muscle in vertical jump (component 24), but on the lateral soleus (lateral) muscle during Dabke (component 18).

All previous figures are shown for barefoot experiments. Figures 10(a) and (b) illustrates the risk factors on the ligaments and muscles for the females subjects using the average values between the considered experiments, at the moment exhibiting the maximum ground reaction force, while wearing high-heeled shoes normally used in the Lebanese folkloric dance Dabke. It is clear when comparing Figures 9 and 10 that jumping with high heels exhibits lower risk factors than the barefoot jump. This can be explained by the fact that the shoe acts like an impact

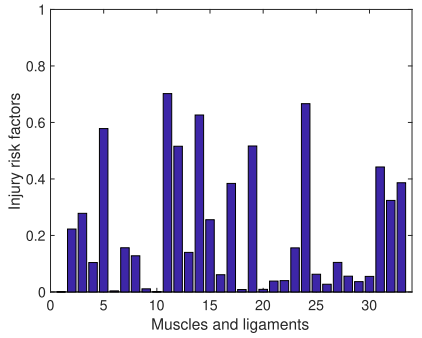

(a) Average risk factors during a vertical jump for males

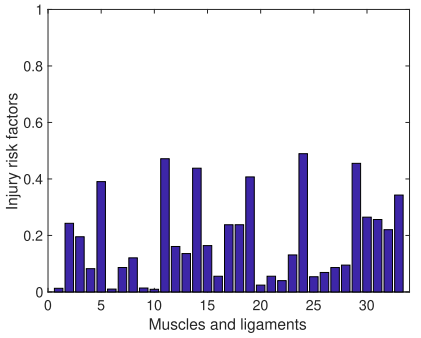

(b) Average risk factors during a Dabke jump for males

Figure 8. Males subjects risk factors using average experimental results with barefoot.

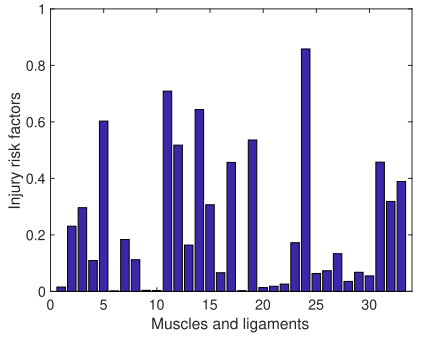

(a) Average risk factors during a vertical jump for females

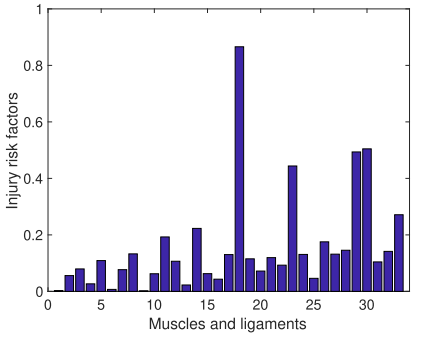

(b) Average risk factors during a Dabke jump for females

Figure 9. Females subjects risk factors using average experimental results with barefoot.

damper during the jump. The highest risk in Dabke for females is still exhibited on the lateral soleus muscle (component 18, while reducing the risk), while in the vertical jump, the risk peak on the Flexor digitorum longus muscle (component 24) is reduced much.

3.2. *Synovial joint reaction forces*

The exhibited force $\mathcal{F}_2$ appearing in (2) is transmitted to the synovial joint. The synovial joint is therefore compressed and sheared to overcome the applied force. The behavior of the synovial joint is modeled in Section 4 to estimate the injury risk in the joint. The vertical reaction forces are illustrated in Figure 11.

In Figure 11, we can see that the barefoot Dabke jump for female exhibits a much lower reaction force than the other type of jumps. Knowing that the experiment is repeated three times, thus it cannot be seen as an outlier value, we can deduce that the females tend to jump differently in Dabke while on barefoot to reduce the impact on the knee. For the remaining experiments, we can deduce that the synovial joint vertical reaction force is higher in a Dabke jump than in a vertical jump.

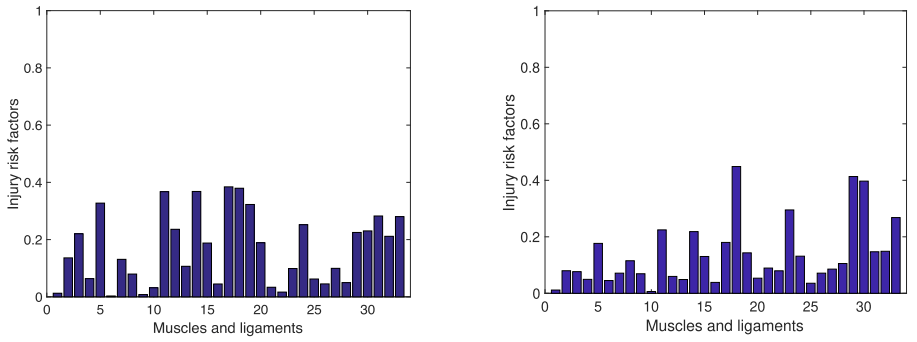

(a) Average risk factors during a vertical jump for females

(b) Average risk factors during a Dabke jump for females

Figure 10. Females subjects risk factors using average experimental results with high-heeled shoes.

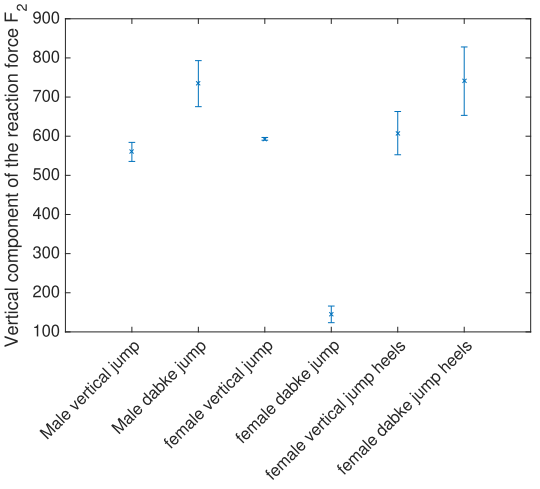

Figure 11. Vertical component of the knee synovial joint reaction force.

4. Simulation of the tibiofemoral joint

4.1. *Brinkman modeling*

In this section, we discuss the modeling of the synovial knee joint. The knee is a biphasic joint whose simplified schematic composition is illustrated in Figure 12. The contribution of the solid component of the porous media in the reaction force is neglected since we are interested in the early stage of the impact. In this modeling, the knee is made of sandwiched biphasic material, supported by two bones. The cartilage and the meniscus are brush-like material [28], impregnated with the synovial fluid. The permeability of the cartilage and meniscus are known to be very low with respect to the rest of the synovial joint [41]. For the sake of simplicity, the meniscus and the articular cartilage are both addressed as "the cartilage" in the rest of the text, with $\Omega_c = \Omega_{c_1} \cup \Omega_{c_2}$, as illustrated in Figure 12.

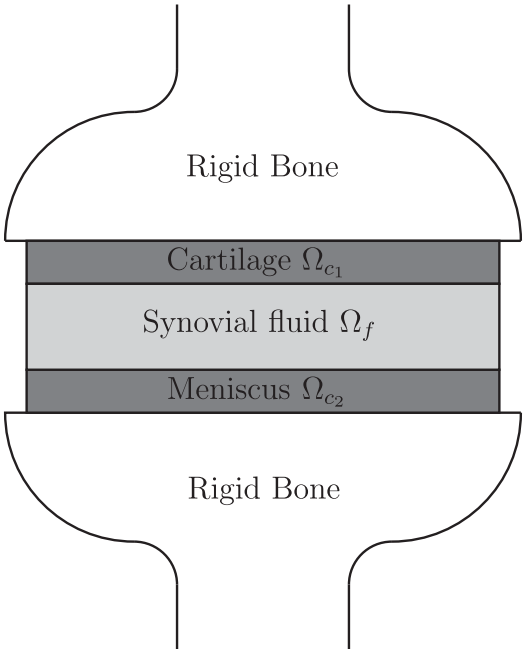

Figure 12. A schematic drawing of the knee joint. The meniscus is considered to also include the lower articular cartilage.

Using the conservation of momentum, an impact can be modeled using an imposed velocity on the knee. Neglecting synovial fluid inertia effects and adopting a quasi-static approach, the impact can be modeled using the steady-state Brinkman equations while neglecting the body forces. Thus, the problem's governing equations are written by

$$\begin{cases} \nabla \cdot \mathbf{v} = 0 \\ \nabla \cdot (\eta \cdot \nabla \mathbf{v}) + \dfrac{\eta}{\mathbf{K}} \mathbf{v} = \nabla P, \end{cases} \tag{4}$$

where η is the fluid viscosity, $\mathbf{v}$ the fluid velocity field in both the synovial fluid and cartilage regions, while P is the pressure field. $\mathbf{K}$ is the permeability tensor inside the domain, which is defined by

$$\mathbf{K} = \Xi(\mathbf{x})\mathbf{K}_c + (1 - \Xi(\mathbf{x}))\mathbf{K}_f \tag{5}$$

with $\mathbf{K}_c$ and $\mathbf{K}_f$ the permeability tensor of the cartilage region and fluid region, respectively. Ξ is a step function defined by

$$\begin{cases} \Xi = 1 & \text{if } \mathbf{x} \in \Omega_c \\ \Xi = 0 & \text{if } \mathbf{x} \in \Omega_f \end{cases} \tag{6}$$

with Ω_c and Ω_f the cartilage and synovial fluid regions, respectively. Therefore, in the synovial joint, the articular cartilage and the fluid joints exhibit a sudden change in the permeability of the domain, which requires an extremely refined mesh to correctly represent the material properties. Thus, the use of the PGD in-plane–out-of-plane decomposition scheme appears as an appealing approach to efficiently simulate the synovial fluid joint.

The synovial fluid permeability tensor is assumed to have a very high value with respect to the cartilage's permeability, such as the solution of the Brinkman equations tends to the solution of the Stokes one inside the fluid region. For instance $\mathbf{K}_f = \alpha \mathbf{I}$, with $\mathbf{I}$ being the identity matrix, and α is constant large enough with respect to $\mathbf{K}_c$. As for the permeability tensor $\mathbf{K}_c$, in the cartilage

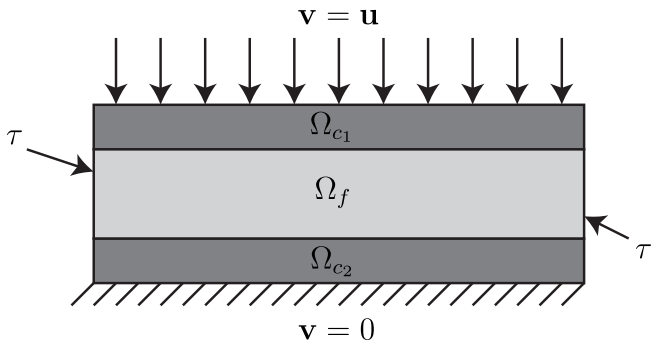

Figure 13. Boundary conditions applied on the knee synovial joint.

region Ω_c, it is identified in different publications [41,42] having an order of magnitude of 10^{-14}, while [43] demonstrated that the in-plane permeability is about one order of magnitude lower than the axial permeability. Therefore the permeability tensor for the cartilage as illustrated in Section 4.2 is

$$\mathbf{K}_c = \begin{bmatrix} 10^{-15} & 0 & 0 \\ 0 & 10^{-15} & 0 \\ 0 & 0 & 10^{-14} \end{bmatrix} m^2. \tag{7}$$

The viscosity of the synovial fluid is considered $\eta = 60$ Pa·s [44], for a normal human being a low shear rate, which is the normal initial equilibrium state as the beginning to the impact reaction. As for the boundary conditions of the problem, the problem consists of an imposed velocity $\mathbf{u}$ on the top of the domain (on the upper bone) and zero velocity on the lower edge of the domain, or the lower bone. Zeros stresses are assumed on the lateral dimensions of the domain

$$\begin{cases} \mathbf{v}(z = H) = \mathbf{u} \\ \mathbf{v}(z = 0) = \mathbf{0} \\ \boldsymbol{\sigma} \cdot \mathbf{n}|_\tau = 0, \end{cases} \tag{8}$$

where H is the domain height and τ the lateral bounds as illustrated in Figure 13. $\boldsymbol{\sigma}$ is the fluid stress tensor and $\mathbf{n}|_\tau$ the outward normal to τ. For the sake of simplicity and since the equation is linear as a function of the imposed velocity $\mathbf{u}$, a velocity $\mathbf{u} = -1 \cdot \mathbf{k}$ can be used, and then the resultant values are multiplied by the corresponding $\mathbf{u}$ value of any experimental testing. The imposed velocity $\mathbf{u}$ is identified by inverse dynamics and optimization, as illustrated in Section 3.

4.2. *PGD solution of the Brinkman model*

In this section, we derive the solution of the governing equation (4) using the PGD. First of all, and because of the lack of efficient treatment of LBB conditions for Brinkman equation in separated representation framework, using the penalty formulation, the conservation of mass is written as [45,46]

$$\nabla \cdot \mathbf{v} = \lambda P \tag{9}$$

with λ a penalty term sufficiently small [45]. The conservation of momentum equation is therefore reduced to

$$\nabla(\nabla \cdot \mathbf{v}) + \lambda \nabla \cdot (\eta \cdot \nabla \mathbf{v}) + \lambda \frac{\eta}{\mathbf{K}} \mathbf{v} = 0. \tag{10}$$

Equation (10) constitutes the governing equation of the problem to solve. Once the velocity is known, the pressure field P would be found by postprocessing using (9). Multiplying (10) by a test function $\mathbf{v}^*$ would give the integral form of the problem to solve in a domain Ω.

$$\int_\Omega \mathbf{v}^* \left(\nabla(\nabla \cdot \mathbf{v}) + \lambda \nabla \cdot (\eta \cdot \nabla \mathbf{v}) + \lambda \frac{\eta}{\mathbf{K}} \mathbf{v} \right) \mathrm{d}\Omega = 0. \tag{11}$$

Along with the boundary conditions depicted in (8), the problem as illustrated exhibits a large discontinuity in the permeability of the domain when passing from the fluid region to the cartilage region, and therefore requires a large number of degrees of freedom in the thickness direction to efficiently illustrate the fluid behavior in the domain. The use of a model order reduction technique becomes a suitable approach in this case.

4.3. *PGD separated representation*

The PGD solution is computed in a cylindrical domain representing the knee synovial joint cavity, assumed with constant radius. Since the domain is extruded, an in-plane–out-of-plane decomposition is appealing in this case. The solution is assumed to be written in a separated form such as

$$\mathbf{v} = \begin{pmatrix} u \\ v \\ w \end{pmatrix} = \begin{pmatrix} \sum_{i=1}^{i=N} U_i^{xy}(x,y) \cdot U_i^z(z) \\ \sum_{i=1}^{i=N} V_i^{xy}(x,y) \cdot V_i^z(z) \\ \sum_{i=1}^{i=N} W_i^{xy}(x,y) \cdot W_i^z(z) \end{pmatrix} \tag{12}$$

with (u, v, w) being the (x, y, z) components of the velocity field $\mathbf{v}$. The test function is assumed to be written in a separated form too [31]

$$\mathbf{v}^* = \mathbf{X}^* \cdot \mathbf{Z} + \mathbf{X} \cdot \mathbf{Z}^*, \tag{13}$$

with $\mathbf{X}^*(x, y)$ the test function in the (x, y) in-plane domain, while $\mathbf{Z}^*(z)$ being the test function in the z out-of-plane domain. Replacing (12) and (13), respectively, into the integral form of the problem (11) leads to a nonlinear problem. The solution is obtained by using an iterative fixed-point algorithm, with rank 1 updates. For instance using $\mathbf{X}_i = (U_i^{xy}; V_i^{xy}; W_i^{xy})$, and $\mathbf{Z}_i = (U_i^z; V_i^z; W_i^z)$, a simplified algorithm will be used to compute vectors $n+1$ knowing the vectors until an order n can be illustrated as follows:

(1) Consider $\mathbf{X}_{n+1}$ as known with the corresponding test function $\mathbf{X}* = \mathbf{0}$, and compute $\mathbf{Z}_{n+1}$.
(2) Consider $\mathbf{Z}_{n+1}$ as known with the corresponding test function $\mathbf{Z}* = \mathbf{0}$, and compute $\mathbf{X}_{n+1}$.
(3) Continue the iterations until convergence of the product $\mathbf{X}_{n+1} \times \mathbf{Z}_{n+1}$.
(4) Keep adding product of functions until convergence of the residual of the differential equation.

Interested reader can refer to the resolution algorithms illustrated in [47] and the references therein.

5. Simulation results

5.1. *A realistic example*

In this section, we illustrate the quasi-real synovial joint by considering the most commonly used dimensions in the literature. Eventually, a real reproduction of the knee joint of any athlete should first consider magnetic resonance imaging to correctly reproduce the shape of the joint. Figure 14

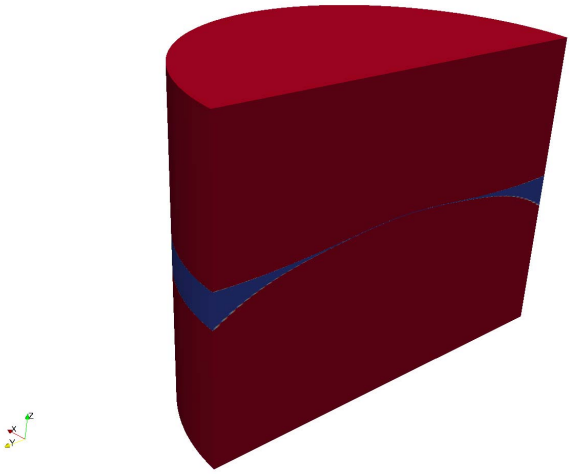

Figure 14. Illustration of the knee real shape considered for the simulation using anthropometric average high of cartilage data. The red region has a low permeability depicted in (7), whereas the blue region is made of synovial fluid with high permeability. The thickness is amplified 10 times to clearly illustrate the domain.

illustrates the considered domain with the average values found in the literature. In fact, using MRI of 20 healthy adults (20 left knees (11 male and 9 female), with an average age of 28.5 years, an average mass of 66 kg, and an average height of 169.6 cm), it was found that the average tibial cartilage thickness is 2.76 mm and the average femoral cartilage thickness is 2.75 mm [48]. Using 3D reconstructed computed tomographic scans from 37 normal adult knees, it was found that the average thickness of the cartilage to be 2.5 mm (SD 1) [49]. In [50], 3D coronal DESSWE MRIs were used to segment and quantitatively measure the size and position of the medial and lateral menisci of 62 women and 40 men. The study showed that the mean medial meniscal height is 2.8 mm for men and 2.55 mm for women and that the mean lateral meniscal height is 2.67 mm for men and 2.51 mm for women [50]. The authors in [51] performed 3−T MR images on 31 women (age 55.3 years (mean, 6 standard deviation)), height 1.62 ± 0.07 m, body mass index 28.0 ± 2.4 kg/m^2), 11 with healthy knee and 20 with radiographic evidence of knee OA [51], where it was found that for the healthy knees the average meniscal thickness was 2.5 mm. Please note that only 0.15 mm separate the meniscus from the upper cartilage before the beginning of the motion. Therefore, we consider 900 nodes in the thickness direction, one element size is therefore about 70 μm, to efficiently reproduce the behavior of the domain.

The definitions of the dimensions of the domain used for the simulations purposes are given in Figure 15 with their corresponding values in Table 2. The upper surface is modeled by a polynomial of degree 4 fitting to the 5 illustrated points, whereas the lower surface is a parabolic fitting of its 3 points. The heights h_1, h_f, and h_3 are, respectively, the heights of the meniscus, the fluid domain, and the upper cartilage domain. The dimensions of the domain are $H = 63$ mm and $R = 80$ mm [52, 53].

The correct representation of the permeability illustrated in Figure 14 is hardly separable in an in-plane–out-of-plane decomposition framework. Many attempts were made to overcome this complication in the literature. The singular value decomposition (SVD) was used in [54] to write the inseparable field in an in-plane–out-of-plane form while only considering the principal components of these fields. Unfortunately, the SVD of the permeability field in our case requires a large number of vector components in the *in-plane* 2D domain and *out-of-plane* 1D domain

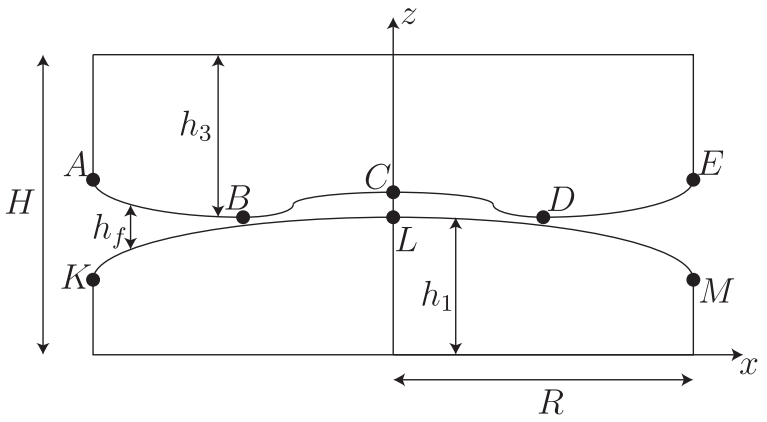

Figure 15. Schematic of the considered control volume. The control volume is revolved around the z axis illustrated in this figure.

Table 2. Positions of the points used to fit the upper and lower interface of the fluid domain in the representative knee joint

Point	x coordinate	z coordinate (mm)
A	$-R$	3.7
B	$-R/2$	3.55
C	0	3.65
D	$R/2$	3.55
E	R	3.7
K	$-R$	2.5
L	0	3.5
M	R	2.5

to correctly represent the permeability fields. Other works attempt to immerse the domain in a larger one [55], or use the polar coordinate system, with an adapted treatment for the singular boundary conditions at the radius $\rho = 0$ [56]. Recently, a physics-based mapping has been introduced in [57] for stratified-like domains, which is suitable for the application illustrated in Figure 14. Using the approach illustrated in [57], we define a mapping of the knee domain $\Omega = (x, y, z)$ with (x, y) a circle of center $(0, 0)$ and radius $R = 4.12$ cm and $z \in [0; 6.3]$ cm, into a prismatic domain $\Omega_s = (X, Y, s)$ with $s \in [0; 3]$ such as

$$\begin{cases} x = X \\ y = Y \\ z = h_1 s\phi_1(s) + \phi_2(s)((s-1)h_f + h_1) + \phi_3(s)((s-2)h_3 + h_f + h_1). \end{cases} \tag{14}$$

h_1, h_f, and h_3 are the height of the meniscus, the fluid region, and the upper cartilage region, respectively, as illustrated in Figure 15. h_1, h_f, and h_3 depends on (x, y), the in-plane coordinates. While $\phi(s)_i$ a step function defined by

$$\begin{cases} \phi_1(s) = 1 & \text{for } s \in [0; 1] \text{ and 0 elsewhere} \\ \phi_2(s) = 1 & \text{for } s \in]1; 2] \text{ and 0 elsewhere} \\ \phi_3(s) = 1 & \text{for } s \in]2; 3] \text{ and 0 elsewhere.} \end{cases} \tag{15}$$

We can therefore define the mapping by part in each of the subdomains Ω_{s_1} for $s_1 \in [0;1]$, Ω_{s_2} for $s_2 \in]1;2]$, and Ω_{s_3} for $s_3 \in]2;3]$. For instance, in subdomain s_i, one may write the Jacobian of the transformation $\mathbf{J}_i$ by

$$\mathbf{J}_i = \begin{bmatrix} \frac{\partial x}{\partial X} & \frac{\partial x}{\partial Y} & \frac{\partial x}{\partial s} \\ \frac{\partial y}{\partial X} & \frac{\partial y}{\partial Y} & \frac{\partial y}{\partial s} \\ \frac{\partial z}{\partial X} & \frac{\partial z}{\partial Y} & \frac{\partial z}{\partial s} \end{bmatrix} = \begin{bmatrix} 1 & 0 & 0 \\ 0 & 1 & 0 \\ \frac{\partial z_i}{\partial X} & \frac{\partial z_i}{\partial Y} & h_i \end{bmatrix} \tag{16}$$

with the determinant of the Jacobian J_i found to be equal to h_i. While the derivatives with respect to the coordinate systems can be updated using the chain rule. For instance for Ω_{s_1}, we can write

$$\begin{cases} \frac{\partial \bullet}{\partial x} = \frac{\partial \bullet}{\partial X}\frac{\partial X}{\partial x} + \frac{\partial \bullet}{\partial Y}\frac{\partial Y}{\partial x} + \frac{\partial \bullet}{\partial s}\frac{\partial s}{\partial x} = \frac{\partial \bullet}{\partial X} + \frac{\partial \bullet}{\partial s}\left(-\frac{\partial h_1}{\partial x}\frac{s}{h_1}\right) \\ \frac{\partial \bullet}{\partial y} = \frac{\partial \bullet}{\partial X}\frac{\partial X}{\partial y} + \frac{\partial \bullet}{\partial Y}\frac{\partial Y}{\partial y} + \frac{\partial \bullet}{\partial s}\frac{\partial s}{\partial y} = \frac{\partial \bullet}{\partial Y} + \frac{\partial \bullet}{\partial s}\left(-\frac{\partial h_1}{\partial y}\frac{s}{h_1}\right) \\ \frac{\partial \bullet}{\partial z} = \frac{\partial \bullet}{\partial X}\frac{\partial X}{\partial z} + \frac{\partial \bullet}{\partial Y}\frac{\partial Y}{\partial z} + \frac{\partial \bullet}{\partial s}\frac{\partial s}{\partial z} = \frac{\partial \bullet}{\partial s}\left(\frac{1}{h_1}\right). \end{cases} \tag{17}$$

We can therefore define the transformation matrix $\mathbf{T}_1$ by

$$\mathbf{T}_1 = \begin{bmatrix} 1 & 0 & \left(-\frac{\partial h_1}{\partial x}\frac{s}{h_1}\right) \\ 0 & 1 & \left(-\frac{\partial h_1}{\partial y}\frac{s}{h_1}\right) \\ 0 & 0 & \left(\frac{1}{h_1}\right) \end{bmatrix}. \tag{18}$$

By similarly defining the matrices $\mathbf{T}_2$ and $\mathbf{T}_3$, we can transform the integration from the Ω domain into Ω_s in the integral form equation (11), obtaining, therefore, a new integral form of the problem

$$\sum_{f=1}^{f=3} \int_{\Omega_{s_f}} \left(\mathbf{v}^* \left(\mathbf{T}_f \nabla_s (\mathbf{T}_f \nabla_s \cdot \mathbf{v}) + \lambda \mathbf{T}_f \nabla_s \cdot (\eta \cdot \mathbf{T}_f \nabla_s \mathbf{v}) + \lambda \frac{\eta}{\mathbf{K}} \mathbf{v} \right) \right) h_i \, \mathrm{d}\Omega_{s_f} = 0. \tag{19}$$

With $\nabla_s \bullet$ defined by

$$\nabla_s \bullet = \begin{pmatrix} \frac{\partial \bullet}{\partial X} \\ \frac{\partial \bullet}{\partial Y} \\ \frac{\partial \bullet}{\partial s} \end{pmatrix}. \tag{20}$$

Solving (19) yields the solution in the transformed domain Ω_s. We can later on apply the mapping illustrated in (14) on the coordinates to find the solution in the knee domain Ω. Interested readers can refer to [57] and its references therein. The solution converges within few minutes on a normal portable PC with 900 nodes in the s mesh, and 2269 nodes in the in-plane mesh, with a total of 6, 126, 300 degrees of freedom in 3D.

Figure 16 illustrates the amplitude of the solution $\mathbf{v}$ in the real (x, y, z) domain, considering a section parallel to the z axis passing by $x = 0$. Figure 17 illustrates the deformation of the domain by the considered vector fields $\mathbf{v}$. The sketched vector field clearly show high-velocity fields in the fluid region and lower one in the cartilage and meniscus regions. The high velocity gradients on the surface of the meniscus and cartilage reflect the high pressure imposed on these surfaces. For instance, the pressure field obtained by postprocessing $\mathbf{v}$ is illustrated in Figure 18. The pressure results exhibit high concentration on the meniscus which illustrates, the regions of the highest

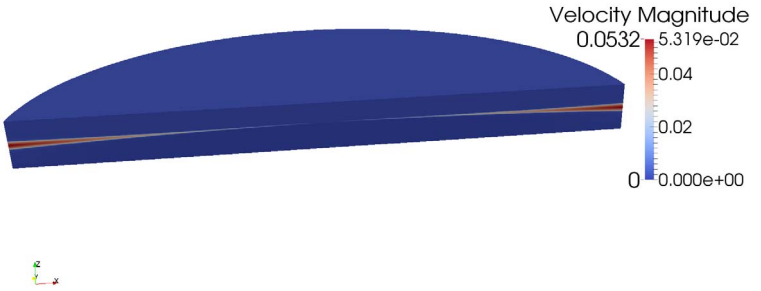

Figure 16. Velocity amplitude field **v** (in m/s) represented in the knee domain Ω, obtained by solving (19) and mapped on the real geometry of the knee joint.

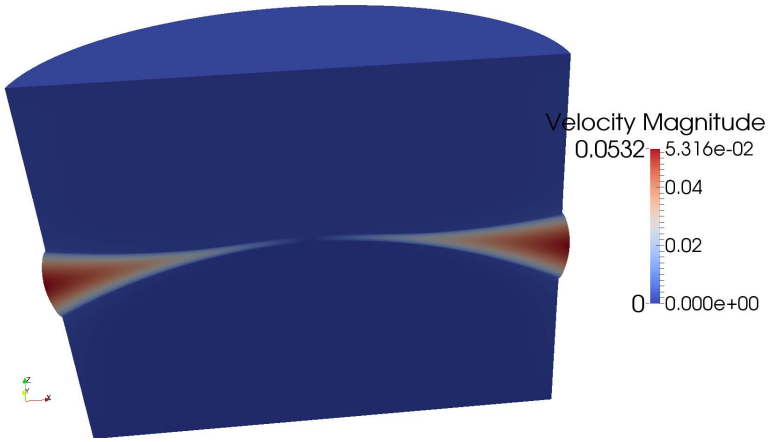

Figure 17. Deformation of the domain Ω by the field **v**, the thickness is amplified by a factor of 10 to illustrate the deformations clearly.

possible injury in the knee synovial joint. The results shown herein are in line with the observed clinical behavior. The high-pressure values can be explained by the selected impact velocity of 1 mm/s and by the sudden change in the permeability of the domains in the simulation. In real life, a tapering region between the meniscus and the synovial fluid may exist with a gradual change in permeability.

Figures 19, 20, and 21 illustrate the shear stresses in the considered domain in the planes (x, y), (x, z), and (y, z), respectively. Again we can notice a high shear stress concentration on the surface of the meniscus.

5.2. *Boundary conditions and experimental results*

In this section, we use the force $\mathcal{F}_2$ to find the impact velocity and thus the pressure and shear for different experimental results. For the impact study, the vertical component of $\mathcal{F}_2$, named $\mathcal{F}_{y_2}$, can be introduced in the linear impulse and momentum equation to find the imposed velocity field **u** on the knee joint. We note that the horizontal component $\mathcal{F}_{h_2}$ is negligible for all experimental results studied. The maximum pressure applied on the knee joint meniscus would thus become

$$P_{\max} = P_{\max@\mathbf{u}=1\,\mathrm{mm/s}} \times \frac{\mathcal{F}_{y_2} \cdot 10^{-3}}{m_{\mathrm{knee}}} \tag{21}$$

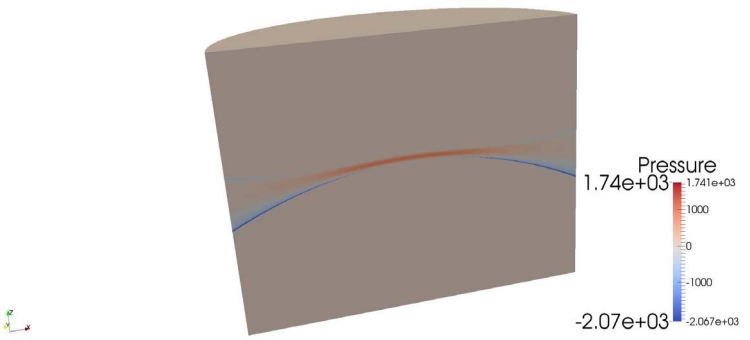

Figure 18. Gaged pressure (in Pa) in the knee joint obtained by postprocessing **v**. The domain thickness is amplified by a factor of 10.

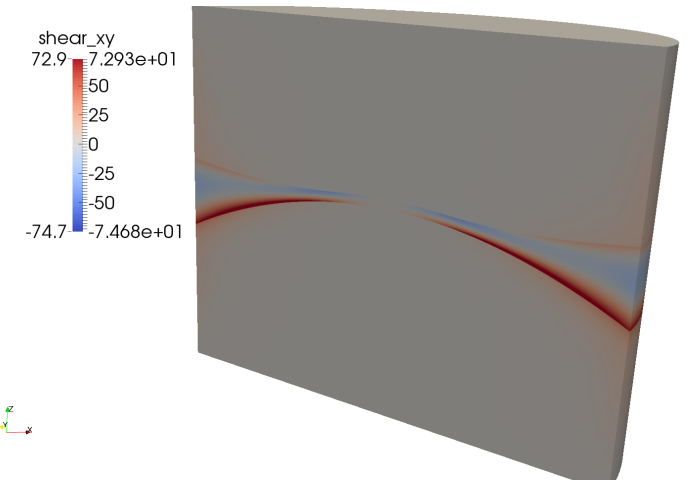

Figure 19. Shear stresses $-\mu((\partial u/\partial y)+(\partial v/\partial x))$.

with m_{knee} the mass of the knee joint only. Equation (21) is a fast and reliable method to assess the risk on the knee joint, with respect to the maximum pressure applied when the patient is in vertical standing position.

The identified maximum pressure is highly localized as illustrated in Figure 18, which could not be captured without the use of the PGD along with the smart morphing of spaces. Moreover, the high pressure is also applied on the outer half of the meniscus, as found in different studies [19, 20]. Most athletic knee injuries involve the meniscus, identified as the most stresses knee joint component in our study, as well as one of the most critical knee components and common source of knee pain and disability in the literature [58].

When comparing experimental results, it appears that the pressure on the meniscus is higher for males and females in vertical jumps than in Dabke jumps. It is also shown that the pressure and shear on the meniscus are higher when wearing high heals than during barefoot jumps. The results are shown in Figure 22. The experimental results show that women tend to have a higher pressure on the knee than men during both the Dabke jump and the vertical jump, while apparently females take the jump differently on barefoot and tend to have higher pressure on the knee synovial joint in the barefoot, and lower pressure with heels. Finally, high heeled tend to

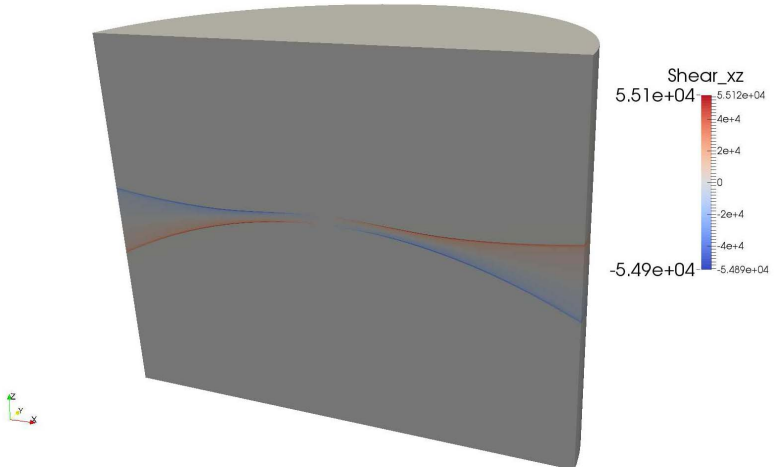

Figure 20. Shear stresses $-\mu((\partial u/\partial z) + (\partial w/\partial x))$.

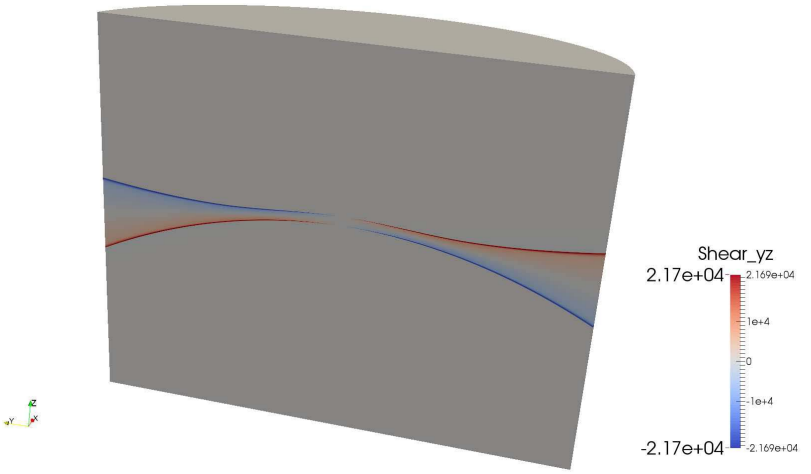

Figure 21. Shear stresses $-\mu((\partial v/\partial z) + (\partial w/\partial y))$.

decrease the pressure on the knees in both Dabke and vertical jumps, working as a damper of the impact.

6. Discussion

The illustrated work is the first attempt to study the Dabke folkloric dance. In the experimental work, we compare the results between the vertical jump and the Dabke dance jump for males and females wearing high heels or barefoot. The highest risk appears to be for barefoot female vertical jumps while considering comparable risk for barefoot Dabke jump in females.

Moreover, the optimization algorithm used in this work is unique to the best knowledge of the authors. No previous optimization in the literature used all the existing muscles and ligaments in its formulation. Moreover, the selected cost function has the advantage of including the ligaments and joint contact forces in the analysis thus improving its predictive ability. Our analysis has

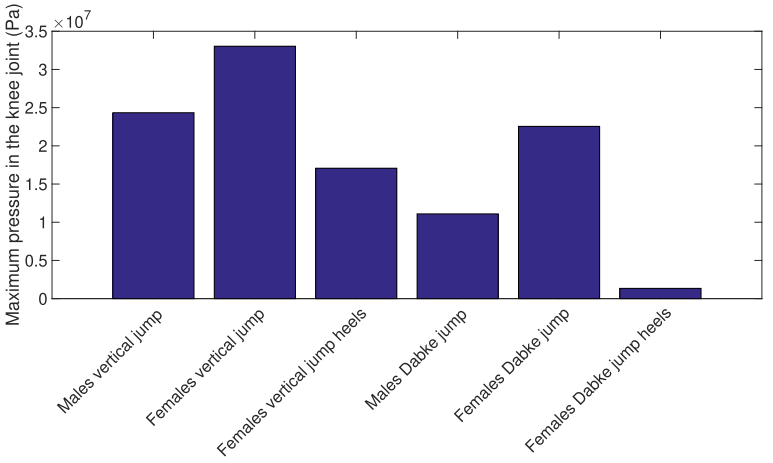

Figure 22. The maximum pressure exhibited in different experimental results.

also the ability to treat exact moment arms of ligament and muscles, considering the through points method for the calculation of the moment arms, instead of an assumption of a straight line between the insertion of the muscles.

Finally, a model of the synovial joint is simulated to find the exact behavior and identify high pressure and shear points, which appears to be concentrated on the upper surface of the meniscus. Eventually, the study cannot be concluded regarding meniscus risk without having a subject specific synovial joint simulation, which would require magnetic imaging of all the subjects performing the experimental tests. The described method is able to simulate the exact meniscus shape for every subject by correctly defining the domain heights, even if the meniscus is not continuous neither symmetrical. However, such approach was not possible since magnetic imaging was not funded for the subjects nor available.

7. Conclusions

This paper introduces a new methodology for assessing joint reaction forces at the knee synovial joint during jumping. This topic has been tackled extensively in the literature, using optimized inverse dynamics (with some simplifications such as omitting some ligament forces or/and some muscle forces etc . . .) coupled with experimental testing that uses as input kinematics and kinetics via motion capture systems (with force plates and EMG). This research proposes a novel method that is (i) coupled with experimental testing to get kinematics and kinetics data as input, (ii) used in any sport application that includes jumping to simulate knee joint reaction forces, (iii) implemented on a light platform such as smartphones or tablets to estimate the risk level during any activity involving jumping.

The proposed methodology consists of the following:

- The novelty of this research and the main contribution of this work is the modeling and simulation of the tibiofemoral knee joint under the impact of jumping using a Brinkman approach for the biphasic synovial joint domain (modeled as a solid mesh and a fluid respectively: cartilage, a meniscus (both a biphasic material) and a synovial fluid). Up to the knowledge of the authors, no one has tackled this problem from this perspective.
- Using inverse dynamics in order to get kinetics at the knee joint (joint reaction forces) based on kinematics (of the all joints, muscles, and ligaments involved in jumping) and kinetics (ground reaction force) inputs.

- Optimizing the kinetics results at the knee joint via including all muscles and ligaments forces (this was simplified in literature, not all components were previously included).
- Using model order reduction technique (PGD) to identify the velocity and pressure fields inside the tibiofemoral joint (never been used before). Once the pressure fields are available, the linearity of the model leverages into a mechanical transfer function approach to identify the maximum pressure in the joint and thus the risk level on the cartilage and meniscus.
- Comparing the Lebanese folkloric dance results to the vertical jumping results for males and females with or without shoes.

Acknowledgments

This work is made possible by the financial support of the Lebanese National Council for Scientific Research Lebanon (CNRS-L). The authors would like to thank the CNRS-L for their research grant. The authors also wish to acknowledge the support of the University Research Board at Notre Dame University-Louaize.

Appendix A. Naming convention of the ligaments and muscles

The naming convention used in this work for the ligaments and muscles from 1 to 33 is explained in Table A.1.

Table A.1. Tests and subjects specific anthropometric data

Number	Name	Number	Name
1	Anterior cruciate ligament	18	Soleus (lateral)
2	Posterior cruciate ligament	19	Patellar ligament
3	Medial collateral ligament	20	tibia.ant
4	Lateral collateral ligament	21	Peroneus.brev
5	Oblique popliteal ligament	22	Peroneus.long
6	Posterior tibiotalar ligament	23	Peroneus.tert
7	Tibiocalcaneal ligament	24	Flex.dig
8	Tibionavicular ligament	25	Flex.hal
9	Posterior talofibular ligament	26	ext.dig
10	Calcaneofibular ligament	27	ext.hal
11	Semimembr.	28	tibia.post (medial)
12	bifemlh	29	Gracilis
13	Rectus fem.	30	Sartorius (prox.)
14	bifemsh	31	Semitend.
15	Vastus med. (inf.)	32	Gastrocn. (medial)
16	Vastus int	33	Gastrocn. (lateral)
17	Vastus lat. (inf.)		

Tests are repeated twice for vertical jumps and Dabke jump.

References

[1] C. Hirsch, V. H. Frankel, "Analysis of forces producing fractures of the proximal end of the femur", *J. Bone Joint Surg.* **42** (1960), no. 3, p. 633-640, British volume.

[2] N. Mezghani, J. de Guise, G. Grimard, D. Baillargeon, Y. Ouakrim, G. Parent, A. Fuentes, P. Lavigne, P. Ranger, "Method and system for knee joint evaluation and diagnostic aid in normal and pathologic state", 3 January 2017, U.S. Patent No. 9,532,732.
[3] D. G. Lloyd, T. F. Besier, "An EMG-driven musculoskeletal model to estimate muscle forces and knee joint moments *in vivo*", *J. Biomech.* **36** (2003), no. 6, p. 765-776.
[4] J. M. Shippen, B. May, "Calculation of muscle loading and joint contact forces during the rock step in Irish dance", *J. Dance Med. Sci.* **14** (2010), no. 1, p. 11-18.
[5] R. Michnik, J. Jurkojć, J. Pauk, "Identification of muscles forces during gait of children with foot disabilities", *Mechanics* **80** (2009), no. 6, p. 48-51.
[6] A. J. Schnorenberg, B. Slavens, M. Wang, L. Vogel, P. Smith, G. Harris, "Biomechanical model for evaluation of pediatric upper extremity joint dynamics during wheelchair mobility", *J. Biomech.* **47** (2014), no. 1, p. 269-276.
[7] C. Quental, J. Folgado, J. Ambrósio, J. Monteiro, "A multibody biomechanical model of the upper limb including the shoulder girdle", *Multibody Syst. Dyn.* **28** (2012), no. 1–2, p. 83-108.
[8] G. Li, K. R. Kaufman, E. Y. Chao, H. E. Rubash, "Prediction of antagonistic muscle forces using inverse dynamic optimization during flexion/extension of the knee", *J. Biomech. Eng.* **121** (1999), no. 3, p. 316-322.
[9] D. J. Cleather, J. E. Goodwin, A. M. J. Bull, "Hip and knee joint loading during vertical jumping and push jerking", *Clin. Biomech.* **28** (2013), no. 1, p. 98-103.
[10] D. J. Cleather, A. M. J. Bull, "An optimization-based simultaneous approach to the determination of muscular, ligamentous, and joint contact forces provides insight into musculoligamentous interaction", *Ann. Biomed. Eng.* **39** (2011), no. 7, p. 1925-1934.
[11] M. Kazemi, L. P. Li, P. Savard, M. D. Buschmann, "Creep behavior of the intact and meniscectomy knee joints", *J. Mech. Behav. Biomed. Mater.* **4** (2011), no. 7, p. 1351-1358.
[12] M. Kazemi, L. P. Li, "A viscoelastic poromechanical model of the knee joint in large compression", *Mech. Eng. Phys.* **36** (2014), p. 998-1006.
[13] G. Li, J. Gil, A. Kanamori, S. L. Woo, "A validated three-dimensional computational model of a human knee joint", *J. Biomech. Eng.* **121** (1999), no. 6, p. 657-662.
[14] T. L. Donahue, M. L. Hull, M. M. Rashid, C. R. Jacobs, "A finite element model of the human knee joint for the study of tibio-femoral contact", *J. Biomech. Eng.* **124** (2002), no. 3, p. 273-280.
[15] M. Freutel, H. Schmidt, L. Dürselen, A. Ignatius, F. Galbusera, "Finite element modeling of soft tissues: material models, tissue interaction and challenges", *Clin. Biomech. (Bristol, Avon)* **29** (2014), no. 4, p. 363-372.
[16] K. B. Gu, L. P. Li, "A human knee joint model considering fluid pressure and fiber orientation in cartilages and menisci", *Med. Eng. Phys.* **33** (2011), no. 4, p. 497-503.
[17] R. Shirazi, A. Shirazi-Adl, M. Hurtig, "Role of cartilage collagen fibrils networks in knee joint biomechanics under compression", *J. Biomech.* **41** (2008), no. 16, p. 3340-3348.
[18] P. N. Tandon, A. Chaurasia, "A porous implant model for a knee joint", *Int. J. Bio-med. Comput.* **29** (1991), no. 1, p. 45-59.
[19] M. Kazemi, L. P. Li, P. Savard, M. D. Buschmann, "Creep behavior of the intact and meniscectomy knee joints", *J. Mech. Behav. Biomed. Mater.* **4** (2011), no. 7, p. 1351-1358.
[20] M. Kazemi, L. P. Li, "A viscoelastic poromechanical model of the knee joint in large compression", *Mech. Eng. Phys.* **36** (2014), p. 998-1006.
[21] M. L. Rodriguez, L. P. Li, "Compression-rate-dependent nonlinear mechanics of normal and impaired porcine knee joints", *BMC Musculoskelet. Disord.* **18** (2017), no. 447, p. 1-10.
[22] C. Ghnatios, F. Chinesta, C. Binetruy, "3D modeling of squeeze flows occuring in composite laminates", *Int. J. Mater. Form.* **8** (2015), p. 73-83.
[23] R. M. Espinosa-Marzal, R. M. Bieleckia, N. D. Spencer, "Understanding the role of viscous solvent confinement in the tribological behavior of polymer brushes: a bioinspired approach", *Soft Matter* **9** (2013), p. 10572-10585.
[24] E. Bonnevie, V. Baro, L. Wang, D. Burris, "Fluid load support during local indentation of cartilage with a spherical probe", *J. Biomech.* **45** (2012), p. 1036-1041.
[25] A. Moore, D. Burris, "An analytical model to predict interstitial lubrication of cartilage in migration contact areas", *J. Biomech.* **47** (2014), p. 148-153.
[26] S. S. Pawaskar, Z. M. Jin, J. Fisher, "Modelling of fluid support inside articular cartilage during sliding", *J. Eng. Tribol.* **221** (2007), p. 165-174.
[27] M. Harris, A. Anderson, C. Henak, B. Ellis, C. Peters, J. Weiss, "Finite element prediction of cartilage contact stresses in normal human hips", *J. Orthop. Res.* **30** (2012), p. 1133-1139.
[28] C. Ghnatios, C. H. Mathis, R. Simic, N. D. Spencer, F. Chinesta, "Modeling soft permeable matter with the proper generalized decomposition (PGD) approach, and verification by means of nanoindentation", *Soft Matter* **13** (2017), p. 4482-4493.
[29] F. Bordeu, C. Ghnatios, D. Boulze, B. Carles, D. Sireude, A. Leygue, F. Chinesta, "Parametric 3D elastic solutions of beams involved in frame structures", *Adv. Aircr. Spacecr. Sci.* **2** (2015), p. 233-248.

[30] E. Cueto, C. Ghnatios, F. Chinesta, N. Montes, F. Sanchez, A. Falco, "Improving computational efficiency in LCM by using computational geometry and model reduction techniques", *Key Eng. Mater.* **611–612** (2014), p. 339-343.
[31] F. Chinesta, A. Ammar, E. Cueto, "Recent advances in the use of the proper generalized decomposition for solving multidimensional models", *Arch. Comput. Methods Eng.* **17** (2010), p. 327-350.
[32] E. H. Garling, B. L. Kaptein, B. Mertens, W. Barendregt, H. E. J. Veeger, R. G. H. H. Nelissen, E. R. Valstar, "Soft-tissue artefact assessment during step-up using fluoroscopy and skin-mounted markers", *J. Biomech.* **40** (2007), no. 1, p. S18-S24, [published correction appears in *J. Biomech.* **41** (2008), no. 10, p. 2332-2335].
[33] R. Dumas, V. Camomilla, T. Bonci, L. Cheze, A. Cappozzo, "Generalized mathematical representation of the soft tissue artefact", *J. Biomech.* **47** (2014), no. 2, p. 476-481.
[34] P. Breitkopf, A. Rassineux, P. Villon, "An introduction to moving least squares meshfree methods", *Meshfree Comput. Mech.* **11** (2002), p. 825-867.
[35] C. Ghnatios, F. Masson, A. Huerta, E. Cueto, F. Chinesta, "Proper generalized decomposition based dynamic data-driven of thermal processes", *Comput. Methods Appl. Mech. Eng.* **213–216** (2012), p. 29-41.
[36] D. A. Winter, *Biomechanics and Motor Control of Human Movement*, John Wiley & Sons, Hoboken, NJ, 2009.
[37] A. Erdemir, S. McLean, W. Herzog, A. Van Den Bogert, "Model-based estimation of muscle forces exerted during movements", *Clin. Biomech.* **22** (2007), p. 131-154.
[38] D. Cleather, A. Bull, "An optimization-based simultaneous approach to the determination of muscular, ligamentous, and joint contact forces provides insight into musculoligamentous interaction", *Ann. Biomed. Eng.* **39** (2011), no. 7, p. 1925-1934.
[39] L. L. Menegaldo, A. De Toledo Fleury, H. I. Weber, "Moment arms and musculotendon lengths estimation for a three-dimensional lower-limb model", *J. Biomech.* **37** (2004), no. 9, p. 1447-1453.
[40] M. D. Klein Horsman, H. Koopman, F. Van Der Helm, L. Poliacu Prose, H. Veeger, "Morphological muscle and joint parameters for musculoskeletal modelling of the lower extremity", *Clin. Biomech.* **22** (2007), p. 239-247.
[41] Y. Wang, H. Meng, X. Yuan, J. Peng, Q. Guo, S. Lu, A. Wang, "Fabrication and *in vitro* evaluation of an articular cartilage extracellular matrix-hydroxyapatite bilayered scaffold with low permeability for interface tissue engineering", *Biomed. Eng. Online* **13** (2014), no. 80, p. 1-18.
[42] A. Maroudas, P. Bullough, "Permeability of articular cartilage", *Nature* **219** (1968), no. 5160, p. 1260-1261.
[43] B. Reynaud, T. Quinn, "Anisotropic hydraulic permeability in compressed articular cartilage", *J. Biomech.* **39** (2006), p. 131-137.
[44] V. Wright, D. Dowson, "Lubrication and cartilage", *J. Anatomy* **121** (1976), no. 1, p. 107-118.
[45] J. Donea, A. Huerta, *Finite Element Method for Flow Problems*, Wiley, 2003.
[46] T. Hughes, W. Liu, A. Brooks, "Finite element analysis of incompressible viscous flows by the penalty function formulation", *J. Comput. Phys.* **30** (1979), p. 1-60.
[47] F. Chinesta, R. Keunings, A. Leygue, *The Proper Generalized Decomposition for Advanced Numerical Simulations*, SpringerBriefs, 2014.
[48] A. Connolly, D. Fitz Patrick, J. Moulton, J. Lee, A. Lerner, "Tibiofemoral cartilage thickness distribution and its correlation with anthropometric variables", *Proc. Inst. Mech. Eng. H* **222** (2008), no. 1, p. 29-39.
[49] F. Iranpour, A. M. Merican, A. A. Amis, J. P. Cobb, "The width: thickness ratio of the patella", *Clin. Orthop. Relat. Res.* **466** (2008), no. 5, p. 1198-1203.
[50] K. Bloecker, M. Englund, W. Wirth, M. Hudelmaier, R. Burgkart, R. B. Frobell, F. Eckstein, "Revision 1 size and position of the healthy meniscus, and its correlation with sex, height, weight, and bone area—a cross-sectional study", *BMC Musculoskelet. Disord.* **12** (2011), no. 248, p. 1-9.
[51] W. Wirth, R. Frobell, R. Souza, X. Li, B. Wyman, M. P. Le Graverand, T. M. Link, S. Majumdar, F. Eckstein, "A three-dimensional quantitative method to measure meniscus shape, position, and signal intensity using MR images: a pilot study and preliminary results in knee osteoarthritis", *Magn. Reson. Med.* **63** (2010), no. 5, p. 1162-1171.
[52] E. Servien, D. Viskontas, B. Giuffre, M. Coolican, D. Parker, "Reliability of bony landmarks for restoration of the joint line in revision knee arthroplasty", *Knee Surg. Sports Traumatol. Arthrosc.* **16** (2008), p. 263-269.
[53] J. L. Xiao, Z. L. Gao, Y. G. Qin, L. Y. L. Zhu, X. Z. Li, T. Liu, "Use of Insall-Salvati ratio and knee joint line positioning by MR imaging to restore joint lines during revision knee arthroplasty in the Chinese population", *Kuwait Med. J.* **48** (2016), no. 1, p. 17-24.
[54] A. Courard, D. Néron, P. Ladevèze, L. Ballere, "Integration of PGD-virtual charts into an engineering design process", *Comput. Mech.* **57** (2016), p. 637-651.
[55] C. Ghnatios, A. Ammar, A. Cimetiere, A. Hamdouni, A. Leygue, F. Chinesta, "First steps in the space separated representation of models defined in complex domains", in *ASME 11th Biennial Conference on Engineering Systems Design and Analysis*, American Society of Mechanical Engineers, 2012, p. 37-42.
[56] C. Ghnatios, G. Xu, A. Leygue, M. Visionneau, F. Chinesta, A. Cimetière, "On the space separated representation when addressing the solution of PDE in complex domains", *Discrete Contin. Dyn. Syst.-S* **9** (2016), no. 2, p. 475-500.
[57] C. Ghnatios, E. Abisset, A. Ammar, E. Cueto, J.-L. Duval, F. Chinesta, "Advanced separated spatial representations for hardly separable domains", *Comput. Methods Appl. Mech. Eng.* **354** (2019), p. 802-819.

[58] P. Lento, V. Akuthota, “Meniscal injuries: a critical review”, *J. Back Musculoskelet. Rehabil.* **15** (2000), no. 2, p. 55-62.